NeuroImage 235 (2021) 118005

Contents lists available at ScienceDirect

NeuroImage

journal homepage: www.elsevier.com/locate/neuroimage

Temporal modes of hub synchronization at rest

F. de Pasquale[a,*], S. Spadone[b], V. Betti[c,d], M. Corbetta[e,f,g,#], Stefania Della Penna[b,#]

[a] Faculty of Veterinary Medicine, University of Teramo, Teramo, Italy
[b] Department of Neuroscience, Imaging and Clinical Sciences, and Institute for Advanced Biomedical Technologies, "G. d'Annunzio" University of Chieti-Pescara, Chieti, Italy
[c] Department of Psychology, Sapienza University of Rome, 00185, Rome, Italy
[d] IRCCS Fondazione Santa Lucia, 00142, Rome, Italy
[e] Department of Neuroscience and Padova Neuroscience Center (PNC), University of Padua, Padua, Italy
[f] Venetian Institute of Molecular Medicine (VIMM), Padua, Italy
[g] Department of Neurology, Radiology, and Neuroscience, Washington University St. Louis

A B S T R A C T

The brain is a dynamic system that generates a broad repertoire of perceptual, motor, and cognitive states by the integration and segregation of different functional domains represented in large-scale brain networks. However, the fundamental mechanisms underlying brain network integration remain elusive. Here, for the first time to our knowledge, we found that in the resting state the brain visits few synchronization modes defined as clusters of temporally aligned functional hubs. These modes alternate over time and their probability of switching leads to specific temporal loops among them. Notably, although each mode involves a small set of nodes, the brain integration seems highly vulnerable to a simulated attack on this temporal synchronization mechanism. In line with the hypothesis that the resting state represents a prior sculpted by the task activity, the observed synchronization modes might be interpreted as a temporal brain template needed to respond to task/environmental demands .

Significance statement

The brain is a hierarchical distributed network characterized by highly integrated peripheral modules connected by a relatively small set of strongly connected central regions (hubs). Hub regions commonly activate across many cognitive tasks suggesting that they operate as a backbone for integrating different cognitive domains depending on task demands. In the temporal domain, however, mechanisms of integration are unknown. We show that hub regions synchronize in different sets, each in turn connected to different peripheral regions. Their alternation in the resting state corresponds to changes in the whole brain's global efficiency, and their damage leads to loss of efficiency. Hub synchronization is, therefore, one mechanism for integrating information across distinct brain networks.

1. Introduction

The brain is an integrated dynamical system that generates flexible and diverse cognitive states through the integration (segregation) of different brain networks that mediate different functions through patterns of synchronized neural activity (Cocchi et al., 2017; Shine et al., 2019). This hypothesis is supported by dynamically changing patterns of connectivity measured with different methods: fMRI/MEG/EEG both at rest and during tasks. Yet, the exact mechanism through which different brain networks dynamically integrate is still a matter of debate.

When the brain is modeled as a metastable system operating in a regime of criticality, efficient integration occurs through continuous temporal fluctuations and synchronization of different connectivity states (Cocchi et al., 2017). These states have been observed at different time scales ranging from the fast dynamics of EEG microstates (Van de Ville et al., 2010) and HMM MEG states (Baker et al., 2014; Vidaurre et al., 2017), to the slow connectivity fluctuations reported in MEG-BLP studies (de Pasquale et al., 2012; de Pasquale et al., 2016), down to the ultraslow fMRI fluctuations (Chang and Glover, 2010; Hutchison et al., 2013) at rest and similarly during task performance (Shine et al., 2016).

On the other hand, network integration includes the notion of cortical hubs. The brain is organized as a hierarchical distributed network organized in densely integrated peripheral modules connected by a relatively small number of a densely connected set of 'central' regions or hubs. Hubs act as waystations of information transfer between peripheral and highly connected areas (de Pasquale et al., 2018). Functional imaging and electrophysiological studies have shown that hubs are commonly activated at rest and during different cognitive tasks (de Pasquale et al., 2018; de Pasquale et al., 2017; de Pasquale et al., 2012; Della Penna et al., 2019; Power et al., 2013; van den Heuvel and Sporns, 2013). In fMRI, hubs can be distinguished based on their spatial topography in the network (Gordon et al., 2018) and their dynamical pattern of integration with other regions (Vatansever et al., 2015). Fur-

* Corresponding author.
E-mail address: fdepasquale@unite.it (F. de Pasquale).
# These senior authors contributed equally to this work.

https://doi.org/10.1016/j.neuroimage.2021.118005
Received 18 November 2020; Received in revised form 12 March 2021; Accepted 17 March 2021
Available online 2 April 2021

thermore, functional hub regions operate in different frequency bands, and their joint centrality fluctuations relate to the efficiency of information transfer suggesting that they may also participate in cross-network integration (Betti et al., 2018; Cole et al., 2013; de Pasquale et al., 2016; Kabbara et al., 2017). Therefore, based on the notion that integration requires communication across different connectivity states alternating in time and characterized by specific central regions, we tested the hypothesis that such integration is realized through the synchronization of these hubs in temporal epochs in which their own centrality is significant. This mechanism – inter-hub synchronization in epochs of high centrality – may therefore integrate different groups of regions that belong to different networks, hence different functional domains. We define these shared dynamics as 'Synchronization Modes'. We tested this hypothesis in a large group of MEG resting-state recordings in healthy subjects. Specifically, we examined the inter-regional dynamical correlation of MEG band-limited power in the alpha and beta bands, where MEG hubs have been mostly reported (Betti et al., 2018; de Pasquale et al., 2012). We examined the existence of synchronization modes, their temporal properties, probability of transition, impact on the overall efficiency of communication, and its vulnerability to a simulated failure of synchronization.

2. Materials and methods

2.1. Subjects and acquisition procedures

A total of 43 healthy young adult subjects (age range = 19–35 years old; 24 females) were scanned with MEG. Each subject underwent two or three resting-state runs (lasting 5 min) for a total of 105 sessions. During the acquisition, subjects maintained fixation on a small visual target. Neuro-magnetic signals (filter settings 0.16–250 Hz, 1025 Hz sampling rate) were recorded using the 153-magnetometer MEG system installed in a 4-layer magnetically shielded room at the University of Chieti (Della Penna et al., 2000). Two ECG and two EOG channels were recorded simultaneously with the MEG signals and were used for offline artifact rejection. After each run, the subject's head position relative to the MEG sensor was estimated from the field produced by five coils placed on the scalp, whose positions were digitized together with anatomical landmarks (nasion, left and right preauricular, vertex) using a 3D digitizer (3Space Fastrak; Polhemus). Structural images, to be used also for MEG processing, were collected using a sagittal M-PRAGE T1-weighted sequence (TR = 8.14 ms; TE = 3.7 ms; flip angle = 8°; voxel size = $1 \times 1 \times 1$ mm^3) on a Philips Achieva 3T scanner.

2.2. MEG data Preprocessing

A full description of our preprocessing pipeline to obtain Band Limited Power (BLP) time series can be found in (Mantini et al., 2011) and it was applied to resting-state (de Pasquale et al., 2010; de Pasquale et al., 2012; Marzetti et al., 2013), and event-related (Larson-Prior et al., 2013; Sebastiani et al., 2014) studies. Here, we summarize the basic steps. First, environmental and physiological (e.g., cardiac, ocular) artifacts were identified from the sensor-space MEG time series using an ICA-based approach and only ICs that were not artifacts were retained for further analysis. However, if the number of non-artifact ICs was <4, possibly indicating excessive movements of the head, the whole run was eliminated. Then, sensor-space signals were projected on a 3D Cartesian grid (64 mm^3 cubic voxels) using a Weighted Minimum Norm Least Square (WMNLS) estimation of the non-artifactual IC sensor maps. For every voxel in the 3D grid, the MEG activity was represented by a current dipole with 3 directions . We assumed that nodes of different RSNs correspond to single MEG voxels. Since the diagonal of our cubic voxel is around 7 mm, the volume of each node is comparable to that of typical ROIs used in fMRI analysis, e.g. 10 mm spheres, see (Stanley et al., 2013) and (Favaretto et al., 2021) for fMRI vs MEG seed-based connectivity comparison. The individual 3D grid was then projected into the MNI 152 atlas space so that every voxel centroid was assigned a set of MNI coordinates. The 3 directions of the MEG activity were obtained at each voxel from the linear combination of IC time courses weighted by the corresponding source maps. Source-space signals were filtered in the alpha [7–14] Hz and beta [14–25 Hz] bands, since in previous studies (Brookes et al., 2011; de Pasquale et al., 2012; Hipp et al., 2012) (de Pasquale et al., 2018; de Pasquale et al., 2016) it was shown that the strongest interactions within/across RSNs occur in these bands. Source-space power time series were estimated over 200 ms windows sliding every 20 ms to cover the entire resting-state run. In this study, the BLP was extracted on a parcellation scheme composed of 155 nodes belonging to 9 RSNs: DAN, VAN, SMN, VIS, AUD, LAN, DMN, FPN, and CON. This set of nodes have been reported in previous studies (Baldassarre et al., 2014; Hacker et al., 2013) and is shown in **Fig. 1A**. In **Table 1** we report their MNI coordinates and labels.

2.3. Connectivity estimation

To obtain leakage-corrected connectomes, each node of the parcellation set was successively taken as a seed and spatial leakage emanating from it was modeled using the Geometric Correction Scheme (GCS) (Wens, 2015; Wens et al., 2015), adapted to our analysis pipeline, as in (Betti et al., 2018; Della Penna et al., 2019). The effects of this approach on connectomes topology with a particular focus on integration measures are extensively analyzed in Della Penna et al. (2019). Briefly, given a seed and the linear inverse operator associated with our source reconstruction pipeline, the GCS provided a set of corrected non-artifactual IC maps. These were used to obtain leakage corrected BLP for all the other nodes in the parcellation set. We first obtained a connectome where each row (corresponding to a seed) was obtained by correlation of the uncorrected BLP obtained at the seed location with the corrected BLP at the other nodes. GCS connectomes were then symmetrized by averaging the upper and lower triangles to account for slight asymmetries induced by numerical approximation. Finally, to remove the contribution of possible local under-correction effects due to seed mislocalization in the GCS connectomes, we masked out node pairs closer than 35 mm.

To obtain a set of dynamic connectomes, transient coupling across the parcellation nodes was estimated through the Pearson coefficient over a time window lasting 10 s and sliding every 200 ms. A time window of 10 s corresponds to the carrier frequency at which the BLP time-series correlation most strongly occurs (~0.1 Hz) (de Pasquale et al., 2010; Hipp et al., 2012). Correlation values were then Fisher transformed and the resulting time-varying connectomes were used for both the static and dynamic analysis.

As far as it regards the static analysis, first, the time-varying connectomes were averaged across time and subjects. These connectomes were then thresholded to the highest z-Fisher values scores leading to a fully connected graph (Bordier et al., 2017). We then estimated the binary Betweenness Centrality at each node. To assess the statistical significance of BC values, we compared them with the BC values obtained from the null model. This was obtained by generating a set of 10000 random graphs preserving the degree distribution (via Brain Connectivity Toolbox, https://sites.google.com/site/bctnet/ Rubinov and Sporns (2010)). From this set of random graphs, we built our BC null distribution and we estimated the corresponding p-values for the real BC values. To correct for the multiple comparisons, we applied the Benjamini–Hochberg procedure to the ranked p-values to control the False Discovery Rate (FDR) at level $\alpha = 0.05$. Nodes surviving the FDR correction were considered as statistically significant static hubs. The above steps were performed in both the alpha and beta bands.

As far as it regards the analysis of dynamics of integration (see **Fig. 1B**) the steps were very similar. First, for every subject, the data from the consecutive runs were concatenated. Then, the binarization of connectomes and BC computation were performed as described above but instead of on average connectomes, at every time point. This led to a temporal sequence of binary BC patterns. In this study, we focused on

Table 1
The adopted brain parcellation. MNI coordinates, node labels, and related networks are reported.

NODE ID	MNI COORDINATES			LABEL	RSN	NODE ID	MNI COORDINATES			LABEL	RSN
	x	y	z				x	y	z		
1	30	-13	53	RFEF	DAN	79	37	-62	-11	RVOIT	VIS
2	-26	-12	53	LFEF	DAN	80	43	-75	-11	RLOMT	VIS
3	23	-69	49	RPIPS	DAN	81	-25	-93	-2	LLO	VIS
4	46	-32	50	RaIPs	DAN	82	42	-80	4	RLOMT	VIS
5	18	-59	53	RdSPL	DAN	83	35	-79	0	RLO	VIS
6	28	-49	52	RSPL	DAN	84	-11	-74	-6	LVP	VIS
7	26	-69	30	RvIPS	DAN	85	17	-64	-5	RVP	VIS
8	-25	-67	48	LpIPS	DAN	86	18	-76	26	RPOSd	VIS
9	-32	-42	45	LaIPS	DAN	87	60	-22	6	RSTG	AUD
10	-22	-53	52	LPreCun	DAN	88	-41	-28	6	LSTG	AUD
11	-31	-80	18	LvIPS	DAN	89	-51	-22	5	LSTG	AUD
12	-43	-72	-8	LMT	DAN	90	-56	-33	16	LINS	AUD
13	42	-70	-11	RMT	DAN	91	-43	-34	11	LSTG	AUD
14	53	-28	36	RSMG	DAN	92	54	-43	12	RSTG	AUD
15	45	-3	34	RvPrCe	DAN	93	-54	-40	10	LSTG	AUD
16	46	-51	-14	Rfus	DAN	94	38	-19	12	RIns	AUD
17	39	30	12	RIFG	DAN	95	-35	-20	14	LIns	AUD
18	-49	-5	32	LvPrCe	DAN	96	34	-24	17	RIns	AUD
19	-40	-42	-19	Lfus	DAN	97	36	0	12	RIns	AUD
20	-45	-34	45	LPoCe	DAN	98	-38	-4	11	LIns	AUD
21	-53	-29	37	LvPoCe	DAN	99	50	-12	17	RPoCe	AUD
22	41	17	31	rSFG	VAN	100	38	-6	4	RCla	AUD
23	12	5	61	rMFG	VAN	101	-37	-8	3	LCla	AUD
24	41	2	50	RMFG	VAN	102	-30	0	15	LCla	AUD
25	52	-48	28	RSMG	VAN	103	-48	31	-1	LIFG	LAN
26	58	-48	10	rSTG	VAN	104	-50	19	9	LIFG	LAN
27	40	21	-4	RIFG	VAN	105	-45	13	24	LMFG	LAN
28	46	11	9	RvIFG	VAN	106	-7	9	60	LSFG	AUD
29	27	50	23	RaPFC	VAN	107	-50	-54	22	LSTS	LAN
30	-57	-48	32	LSMG	VAN	108	-56	-12	-3	LSTG	LAN
31	5	-22	40	RAC	VAN	109	-55	-48	15	LaSTG	LAN
32	30	8	-5	RAI	VAN	110	-48	-44	3	LpMTG	AUD
33	-44	10	8	LvIFG	VAN	111	-56	-33	3	LMTG	AUD
34	42	28	1	RIFG-AI	VAN	112	-52	-54	12	LAG	AUD
35	-33	17	-5	LAI	VAN	113	-54	-23	-3	LSTG	AUD
36	-10	-32	43	LPC	VAN	114	47	25	-4	RIFG	AUD
37	39	11	21	RvPrCe	VAN	115	44	-36	6	RSTG	AUD
38	-60	-28	24	LSII	SMN	116	53	23	7	RpIFG	AUD
39	35	-26	55	RCS	SMN	117	61	-43	8	RpSTG	AUD
40	56	-2	23	RPrCe	SMN	118	2	53	24	RdmPFC	DMN
41	-37	-19	53	LCS	SMN	119	-2	51	2	LvmPFC	DMN
42	-57	-8	21	LPoCe	SMN	120	-13	52	23	LdPFC	DMN
43	57	-28	23	RSII	SMN	121	-2	40	27	LdmPFC	DMN
44	-1	-17	55	LSMA	SMN	122	-3	-54	31	LPCC	DMN
45	-10	-12	60	LdSMA	SMN	123	51	-64	32	RAG	DMN
46	-12	-20	40	LvSMA	SMN	124	-43	-76	35	LAG	DMN
47	4	-15	53	RSMA	SMN	125	-57	-25	-17	LITG	DMN
48	10	-33	52	RParaCe	SMN	126	8	-51	29	RPrecun	DMN
49	-30	-18	10	LPUT	SMN	127	0	-65	31	Cun	DMN
50	30	-17	9	RPUT	SMN	128	-1	44	-2	LACC	DMN
51	-42	-17	46	LcPrCe	SMN	129	-4	42	45	LmSFG	DMN
52	24	-34	60	RdPoCe	SMN	130	-19	22	52	LSFG	DMN
53	-24	-32	63	LdPoCe	SMN	131	17	24	51	RSFG	DMN
54	-54	-23	37	LvPoCe	SMN	132	13	40	40	RSFG	DMN
55	54	-18	37	RvPoCe	SMN	133	59	-25	-12	RMTG	DMN
56	-24	-20	70	LdPrCe1	SMN	134	-5	31	-4	LACC	DMN
57	-44	-9	15	LmI	SMN	135	-9	36	8	LACC	DMN
58	22	-18	58	RdPrCe	SMN	136	-3	28	55	LmSFG	DMN
59	11	-46	59	RSPL-preCun	SMN	137	52	-1	-25	RMTG	DMN
60	-18	-36	55	LParaCe	SMN	138	-6	16	63	LSFG	DMN
61	-7	-44	56	LParaCe	SMN	139	42	10	-29	RSTG	DMN
62	9	-43	53	RParaCe	SMN	140	-41	7	-31	LMTG	DMN
63	11	-92	6	RV1	VIS	141	-31	-59	42	LSPL	FPN
64	-3	-101	0	LV1v	VIS	142	30	-61	39	RPrecun	FPN
65	-8	-88	-7	LV1v	VIS	143	51	-47	42	RIPL	FPN
66	14	-96	14	RV2	VIS	144	10	-69	39	RPrecun	FPN
67	-7	-99	7	LV2	VIS	145	-43	22	34	LPrG	FPN
68	28	-89	15	RV3	VIS	146	-9	-72	37	LPrecun	FPN
69	-16	-93	18	LV3	VIS	147	43	22	34	RPrG	FPN
70	27	-71	-14	RV4	VIS	148	-41	3	36	LPrG	FPN
71	-31	-77	-17	LV4	VIS	149	-51	-51	36	LIPL	FPN
72	32	-78	25	RV7	VIS	150	-28	51	15	LSFG	FPN

(*continued on next page*)

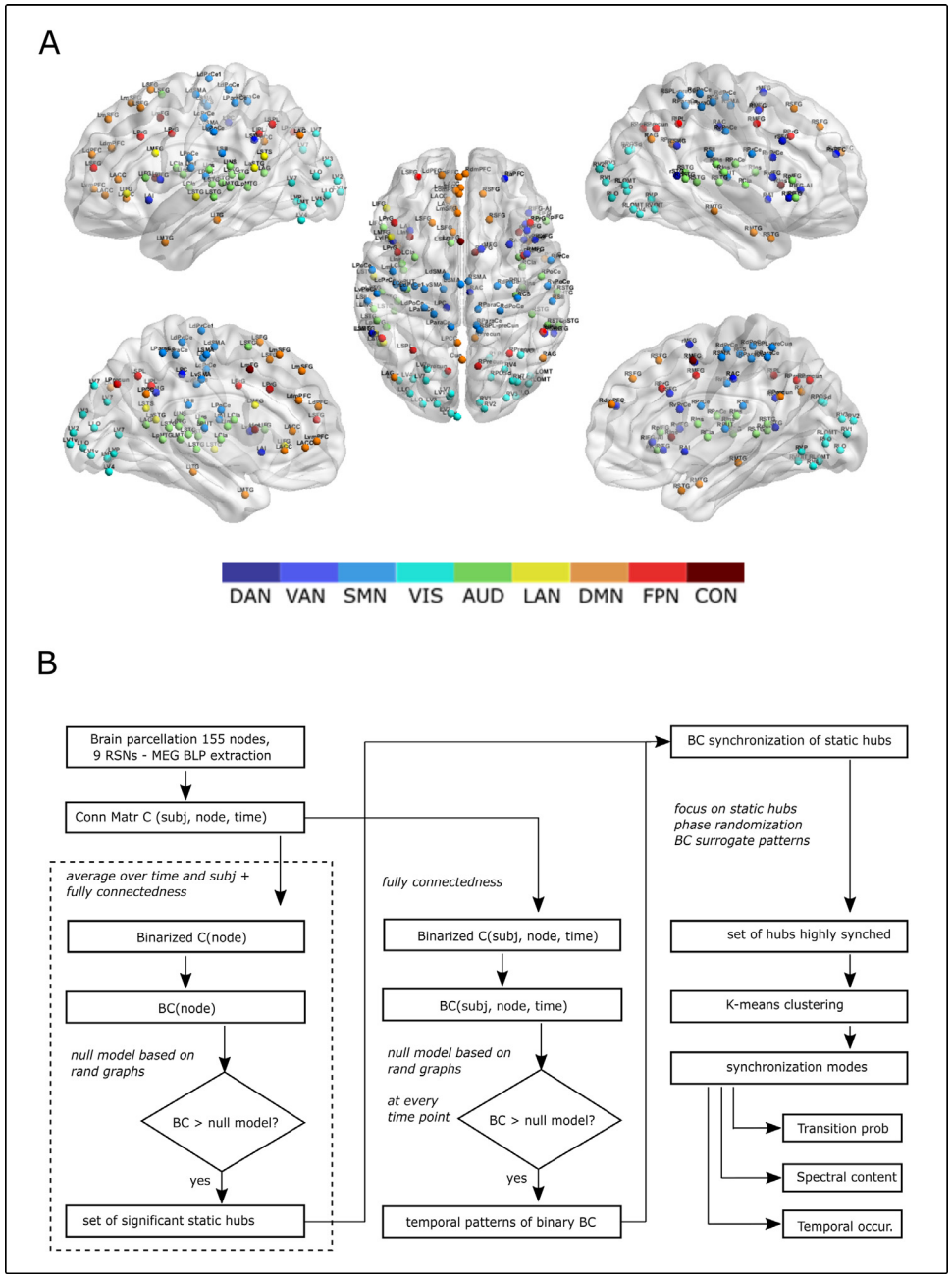

Fig. 1. Analysis Pipeline. A) The adopted brain 155 node-parcellation scheme from 9 RSNs: Dorsal/ Ventral Attention (DAN/VAN), Somato-motor (SMN), Visual (VIS), Auditory (AUD), Language (LAN), Default Mode (DMN), Fronto-Parietal (FPN) and Control (CON). For a complete list of nodes and labels, see **Table 1**. B) A diagram of the analysis steps involved from the pre-processing to the final synchronization mode estimation. The analysis for the estimation of static hubs is highlighted in a dotted box.

Table 1 (*continued*)

NODE ID	MNI COORDINATES			LABEL	RSN	NODE ID	MNI COORDINATES			LABEL	RSN
	x	y	z				x	y	z		
73	-23	-78	26	LV7	VIS	151	39	1	42	RMFG	FPN
74	-7	-86	36	LV7	VIS	152	-33	13	9	LIns	CON
75	-22	-71	6	LV7	VIS	153	36	16	4	RIns	CON
76	34	-88	-4	RLO	VIS	154	-1	10	46	LmFG	CON
77	-40	-78	-9	LMT	VIS	155	8	3	51	RMFG	CON
78	-33	-86	10	LLO	VIS						

the binary BC timecourses since we are interested in identifying time epochs of synchronized high centrality, i.e. the eventual overlap among epochs when the static hubs are highly central (they share BC peaks) or not central at the same time. For this reason, we first extracted the significantly high BC values and then we studied their synchronization. Alternatively, we could have used the original non-binarized BC data and adopted, for example, the correlation as a distance metric. However, this might have been inflated by the joint fluctuations of BC intermediate values which do not contribute to our definition of a synch mode.

Next, we focused on the synchronization of the "static hubs" previously obtained, i.e. we discarded the remaining nodes from the subsequent analyses. Specifically, we adopted a two-step analysis.

First, we identified among the static hubs, a subset of hubs showing a significant pairwise synchronization and then we performed on them a clustering procedure to group those showing a similar synchronization pattern, obtaining a Sync Mode (SM). To identify hubs consistently synchronized, based on their binary BC time-courses, we estimated a SYNC matrix in terms of ROC accuracy (see (Fawcett, 2006)) defined as:

$$SYNC = \frac{TP + FP}{TP + FP + TN + FN}$$

where for a pair of nodes, TP (TN) represents the number of times that BC is 1 (0) at the same time; FP (FN) represents the number of times BC is 1 (0) for the first node and 0 (1) for the second one. Thus, SYNC is a symmetric measure, i.e. does not depend on the order of the considered nodes and considers the proportion of events where the two binary patterns are either on or off divided by the total number of events. Now to identify significant SYNC values we proceeded as follows. First, for every node, from the original BC timecourse, we generated surrogated data through a phase randomization technique Prichard and Theiler (1994). This allows accounting for the autocorrelation (ACF) of the time series. We Fourier transformed the original data, we randomly shuffled the Fourier phases series, and then we anti-Fourier-transformed back the data. This allows obtaining 1000 surrogate replicates with the same ACF as the original one. Then, using the same approach as for the real data, we binarized each replicate and computed the corresponding SYNC matrix. This leads to a sample of 1000 SYNCH matrices that can be used to estimate the null distribution of the synchronization. From this distribution, we estimated the *p*-values of the real BC data and we applied the Benjamini–Hochberg procedure to control the FDR at $\alpha = 0.05$ to mask the significant values in the SYNC matrix.

Then, we focused on this set of hubs, and to identify the final synchronization modes, we performed a K-means clustering on their original BC time-courses driven by SYNC as the distance among observations. To estimate the optimal number of clusters, we run the clustering algorithm corresponding to a variable number of classes. For each output, we computed a mixed performance criterion (MPFC, see (Sinibaldi et al., 2018; Spadone et al., 2012)), which is the product of different clustering performance criteria:

$$MPFC = \frac{CS * AS * DI}{DB}$$

where *CS* is the average cluster size, AS is the average silhouette, DI is the Dunn Index and DB is the Davie Bouldin parameter. In this way, several aspects can be combined and considered in the clustering optimization. The cluster size tends to penalize solutions with many small clusters, while AS, DI, and DB relate to different measures of intra vs inter-clusters distances. A detailed discussion on these aspects can be found in (Spadone et al., 2012).

To analyze the temporal properties of the SM we proceeded as follows. First, we extracted for every synch mode a binary temporal pattern of occurrence, i.e. a pattern that is 1 when all the involved hubs are significantly central ("ON" epochs) and 0 elsewhere. Then, we estimated over time the lag between successive 1 s for every subject and run. If consecutive ON epochs occurred, then the center of each ON interval was considered to estimate the temporal distance of occurrence. This implies that the minimum temporal distance between successive 1 s was 0.4 s. Then, we computed the distribution of the temporal lags and we performed a statistical test (Student's t-test) across runs for every considered distance bin. This test was performed for every pair of modes.

Finally, we computed the probability of transition among states by counting from the binary mode patterns, the number of times in a mode a transition ON/OFF is chronologically followed by a transition OFF/ON of a different mode. The probability is obtained by normalizing this number of times by the total number of transitions.

To study the impact on the overall integration within the network, we adopted the Global Efficiency (GE), defined as the average inverse shortest path length in the network, which is inversely related to the characteristic path length (see (de Pasquale et al., 2016) for more details). Based on GE, we computed the Vulnerability (defined as $(GE-GE_{attack})/GE$) of the graph, to simulate an attack to the involved SM nodes (Kabbara et al., 2017), as follows. For every SM we extracted the sequence of connectomes during the ON epochs. Then, as far as it regards GE, for a given SM, we performed a t-test between the average GE computed during the ON epochs and the corresponding value obtained during all the other temporal epochs. As far as it regards the vulnerability, we considered two different scenarios. In the first case, we considered the dynamics of each SM and we studied the importance of the synchronization of the SM nodes during their ON epochs as compared to the contribution of a selection of random hubs during the same temporal sequence. Although is not unexpected that to attack synched hubs will lead to a higher damage than a random selection of hubs which are not necessarily synched, it is important to quantify this difference. To this aim, for each ON epoch, we replaced the connections of the SM hubs with those from a set of random nodes uniformly sampled from the set of the remaining hubs (either independent or from other SMs). To assess the statistical significance, we performed a paired t-test between the vulnerability obtained from "SM-attacked" and "control-attacked" connectomes.

However, the above analysis does not address the significance of the temporal synchronization of SM hubs. In fact, the random hubs are not necessarily synched in the considered epochs while SM nodes are all central by construction. For this reason, we built a fake synched mode as follows. First, given an SM composed of *n* hubs, we searched for temporal epochs (FAKE-ON epochs) where a set of *n* control hubs, sampled from the set of static hubs, were simultaneously central. These controls were sampled by excluding nodes in the SM and any overlap between FAKE-ON and ON-epochs. Now, since the controls are not part of an SM, and thus their synchronization is not consistent over time, the random selection was repeated at every session potentially leading to the contribution of different hubs. Further, to obtain stable results we replicated this step 100 times within each session. This led to a "fake" SM consisting of sets of random hubs with their epochs of synchronization. For every epoch, we attacked the network by removing the connections involving the nodes of the fake SM. We performed the same attack on the real SM during its ON epochs and then we tested the difference of vulnerability obtained from the two attacks (real vs fake SM). If this difference is significant, this means that GE is damaged more when the real SM is attacked as compared to the fake one. Of note, in this analysis, we account for the different random configurations of connectivity happening over time when a set of nodes are simultaneously central as compared to the same configurations characterizing the synchronization epochs of a mode.

Finally, to analyze the spatial architecture of connections associated with each SM, we computed the average connectome during the related ON epochs. Since the original connectomes were binarized using the full connectedness criterion (see above), this average connectome will provide us with the proportion of time that each connection is observed during the considered synchronization mode. Thus, to extract the most consistent and robust connections, we thresholded this average connectome to its 95th percentile. This binary connectome will represent the most stable connections during each synchronization mode. The graph visualization was realized by using Gephi 0.9.2 (www.gephi.org, (Bastian et al., 2009)).

3. Results

3.1. Static Hub topography

First, we identified a set of nodes that showed over time the most consistent and statistically significant BC. This step was based on a null model built on random graphs so that the adopted threshold was data-driven (see Materials and Methods). We performed these analyses in the alpha and beta bands. **Fig. 2** shows the hub regions in the beta

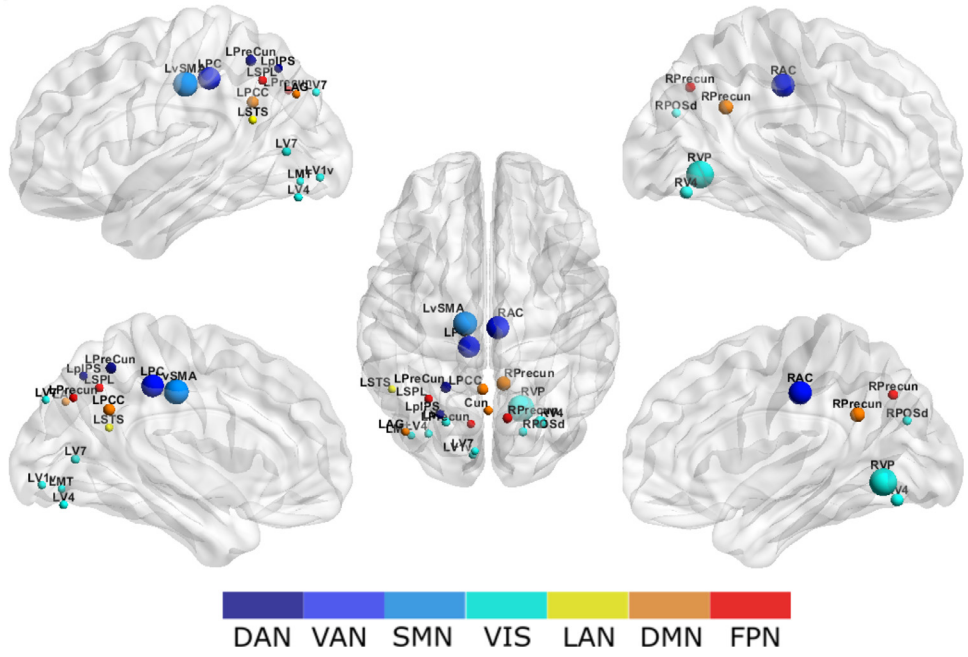

Fig. 2. Functional hubs in the beta band. Location of the most significant 21 functional hubs defined in terms of Betweenness Centrality (BC) obtained from MEG BLP in the beta band. Nodes are color-coded based on the network they belong to and the size of the marker is scaled to the amplitude of BC. The set of hubs is composed of 38% VIS, 20% DMN, 14% FPN, 9% DAN/VAN, and 5% SMN/LAN. It can be noted that this set of nodes includes the nodes (LPCC, LvSMA, and LpIPS) previously reported in (de Pasquale et al., 2012).

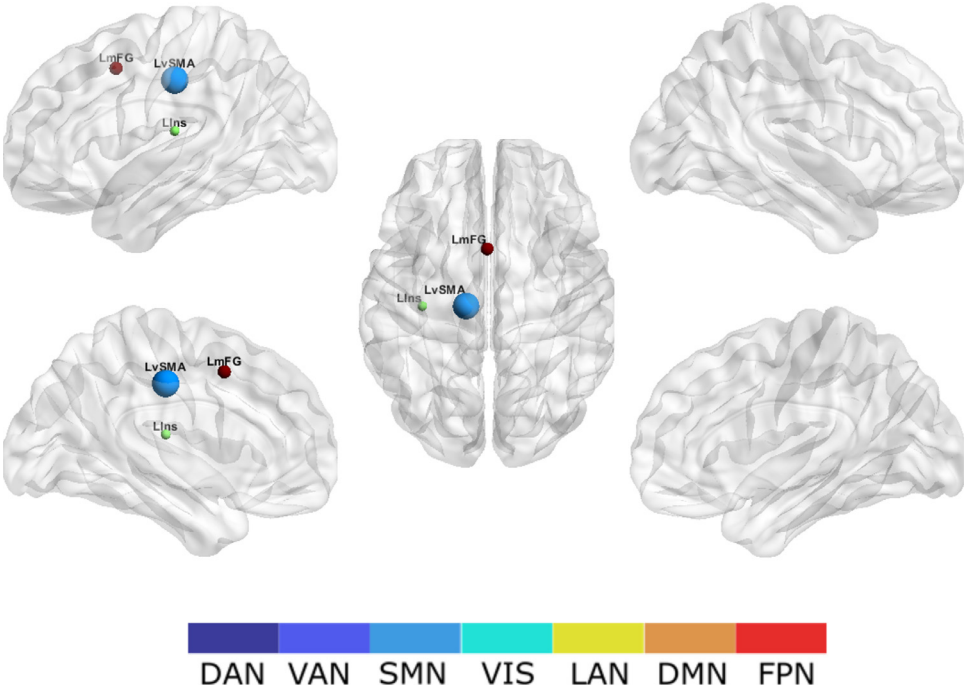

Fig. 3. Functional hubs in the alpha band. The results of the same analysis reported in Fig. 2 are reported for the BLP filtered in the alpha band. A smaller set of functional hubs, namely 3, was obtained and the only overlap between the two sets is in LvSMA (SMN) (see Table 1).

band (nodes are color-coded based on their RSN membership). In this large set of hubs (n = 21), most nodes (38%) were localized in the VIS network, followed by DMN (20%), FPN (14%), DAN/VAN (both 9%), and SMN/LAN (both 5%). The region with the strongest centrality was the left Supplementary Motor Area - LvSMA (Table 1) part of the SMN. Three of these hub regions: LvSMA, LPCC (DMN), and LpIPS (DAN) were reported as 'central' in previous studies (de Pasquale et al., 2012; de Pasquale et al., 2016) using a different approach based on a smaller sample and graph size, different centrality metrics, and leakage-uncorrected data (see (Della Penna et al., 2019) for the effect of leakage correction on the topography of hubs). Thus, this subset of hub regions is stable across subjects, centrality measures, and processing strategies. Further, these results are frequency specific: in the alpha band, the same analysis yielded a smaller (n = 3) set of hub regions (Fig. 3), with one node (LvSMA (SMN)) in common with those found in the beta band. The larger number of central regions in beta than the alpha band is consistent with the previously reported prominent role of the beta band in the brain integration, see (Betti et al., 2018; Betti et al., 2021; de Pasquale et al., 2012; Hipp et al., 2012).

3.2. *Temporal modes of hub synchronization*

Next, we examined hub regions that showed synchronous centrality over time, i.e. they share the same temporal pattern of centrality, and we clustered them based on their BC temporal pattern. Specifically, for every identified hub reported in Fig. 2, based on a bootstrap procedure, we extracted the binarized BC time-course (Fig. 4**A**) (see Materials and Methods for the details). Based on the binary BC dynamics, we estimated

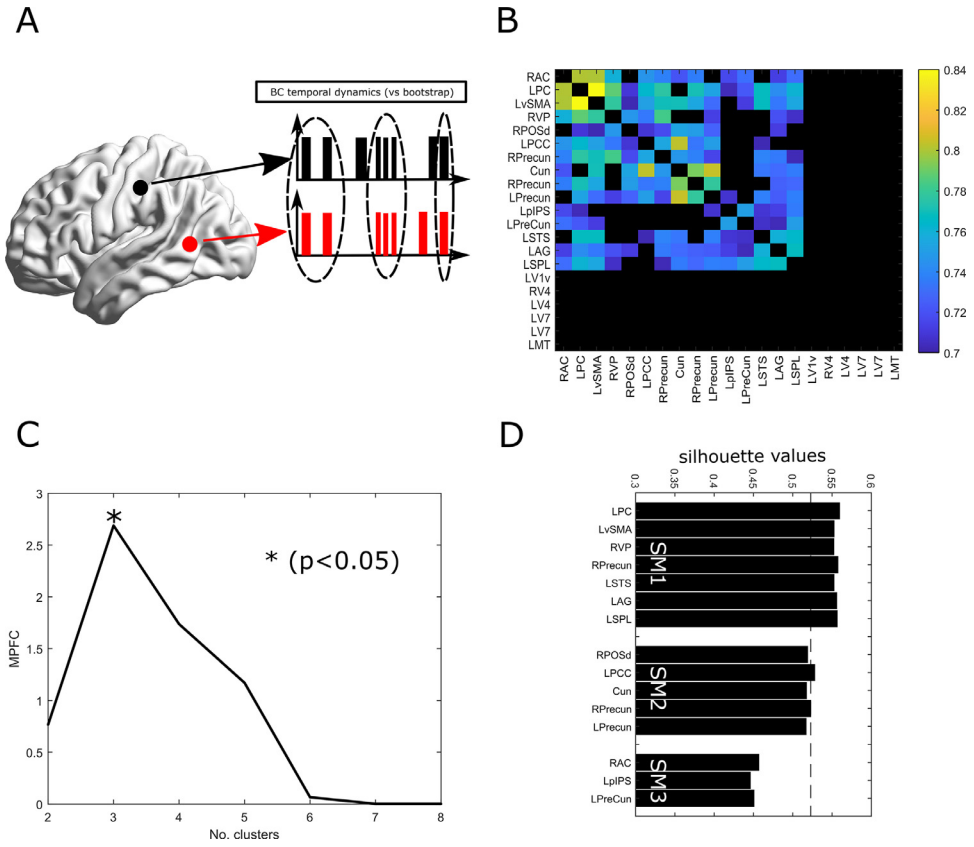

Fig. 4. Synchronization analysis. A) As an example, we display the binary time patterns of BC extracted from two brain nodes used to compute the SYNC matrix (see Materials and Methods). B) The obtained SYNC matrix, nodes reported in black did not show a significant synchronization. C) The Mixed Performance Criterion (MPFC) (see Materials and Methods) adopted to estimate the optimal number of classes for the k-means procedure, shows a clear peak at 3 clusters. This peak resulted significantly different ($p<0.05$) from both the value obtained at 2 and 4 clusters. D) The silhouette analysis of the obtained clusters seems to suggest a good quality of the final clusters since no negative values are obtained, in each cluster the values are close to the average silhouette (dotted line). SM3 shows a slightly smaller silhouette as compared to SM1 and SM2.

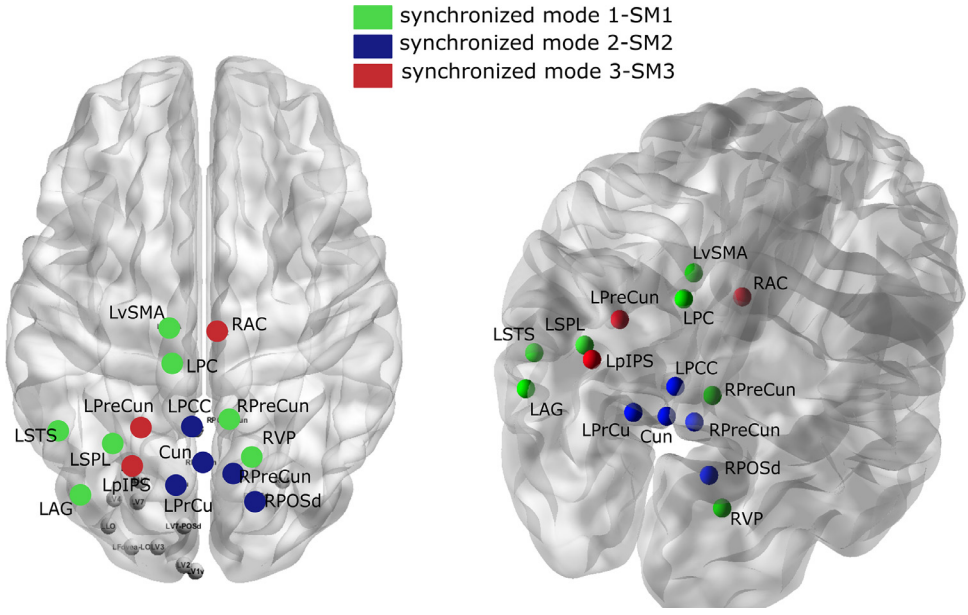

Fig. 5. Synchronization Modes. A) The spatial topography of synchronization modes overlaid to an MNI 152 template. Hubs labeled as independent are shown in gray. Synchronized mode SM1 (green) comprises 6 RSNs and is composed of LvSMA (SMN), RPreCun and LAG (DMN), LSPL (FPN), LSTS (LAN), LPC (VAN), and RVP (VIS). SM2 (blue) is mainly composed of nodes from the DMN, FPN, and VIS such as LPCC and Cun (DMN), RPreCun, and LPrCu (FPN), and RPOSd (VIS). SM3 (red) involves LPreCun and RAC (VAN) and LpIPS (DAN).

the synchronization (SYNC) matrix, reported in Fig. 4**B**. Notably, most hubs in the VIS network did not show any significant synchronization (Fig. 4**B** black, Fig. 5 gray nodes) and were removed from subsequent analyses. On the remaining 15 nodes, we ran K-means clustering driven by the BC timecourses. The optimal number of clusters was obtained by adopting a multi-performance criterion (MPFC) that showed a clear peak corresponding to 3 clusters (see Fig. 4**C,** see Materials and Methods). This value is statistically significant with respect to random fluctuations of the k-means algorithm ($p < 0.05$). However, since MPFC is defined as the product of different parameters depending on the data size and on many other factors, a general reference value to be used as a comparison to assess the quality of the final clustering does not exist. To address this aspect, in Fig. 4**D**, we report the silhouette for the obtained three clusters. These results show that no member has been assigned to a wrong cluster (negative silhouette), members in each cluster have a similar distance as compared with the other members in the same cluster, the values for synch mode 1 and 2 are close to the average silhouette (dotted line). As far as it regards synch mode 3 its silhouette values are slightly below the average value but still all positive. These findings seem to indicate the good quality of the final clustering.

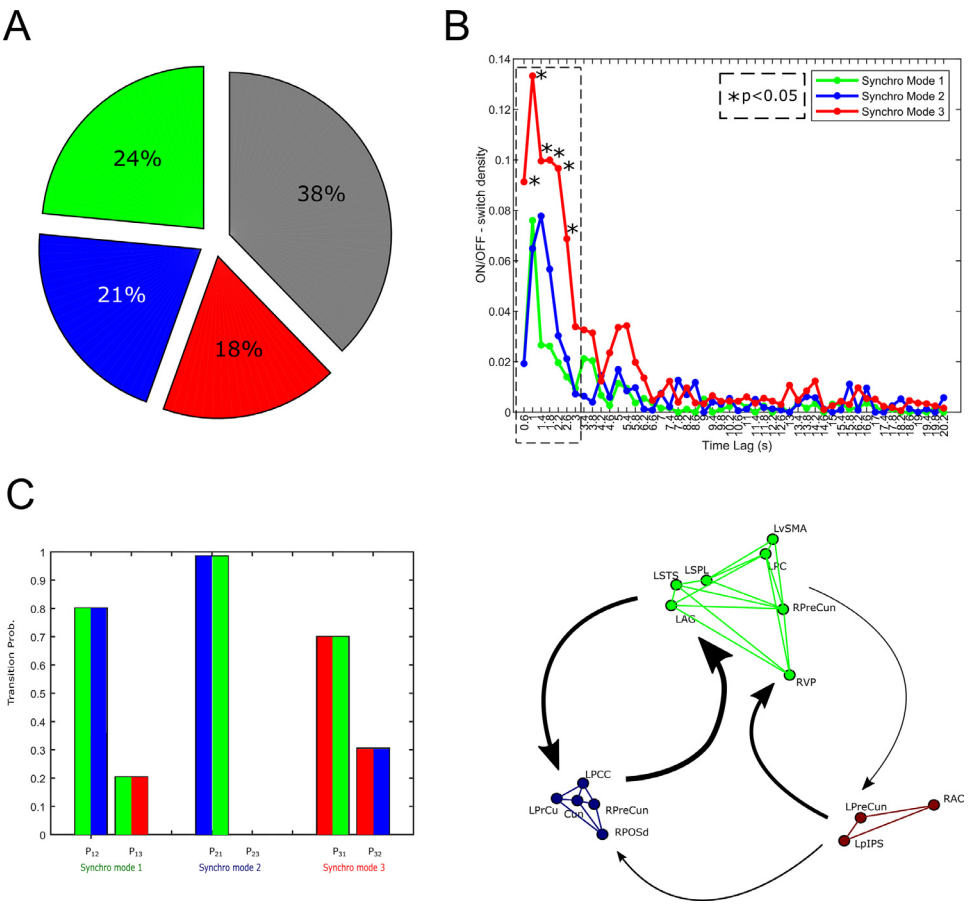

Fig. 6. Temporal characteristics of Synch Modes. A) Synch modes show a similar temporal occurrence: SM1 is ON 24% (green), SM2 21% (blue) and SM3 18% (red). The amount of time no mode is ON corresponds to 38% (grey). B) Distribution of the time lags between ON epochs (see Materials and Methods) of SM1 (green line), SM2 (blue line), and SM3 (red line). The synchro modes 1 and 2 share a similar temporal alternation of ON epochs while SM3 has a significantly higher occurrence at short intervals (dashed box). C) Transition probabilities among synch modes. The switching among modes is not uniform: from SM1 it is very likely to switch to SM2 (P_{12} = 0.8). Once in SM2 is almost certain to get back to SM1 (P_{21} = 0.99). This suggests a predominant loop between SM1 and SM2, highlighted by the thick arrows of the right panel. However, although less frequent, SM3 is basically only reached with a 20% probability from SM1. Once in SM3, the transition towards SM1 is more likely (around 70%) than to SM2 (around 30%). In the right panel, the thickness of the arrows corresponds to the amplitude of the transition probability.

The hub regions belonging to each cluster are shown in Fig. 5. Since these clusters represent groups of hubs highly synchronized over time, i.e. with a similar centrality dynamic, we denote them as 'synchronized modes' (SM) SM1, SM2, and SM3. Every SM is thus represented by a specific spatial topography and a temporal pattern. The topography consists of the location of the involved hubs and their most stable connections. The temporal pattern is defined by the binarized timecourse where the value 1 corresponds to a period of common high centrality (ON epochs) while the value 0 corresponds to periods of common low centrality (OFF epochs). By construction, SMs are not exactly mutually exclusive, and thus their temporal patterns might show some overlap. For this reason, we computed their temporal overlap that resulted exiguous, namely 4% between SM1-SM2, 10% between SM1-SM3, and 11% between SM2-SM3. However, we removed the overlapping epochs in the next analyses so that SMs could be treated as independent. Synchronized mode SM1 (Fig. 5 green) included hub regions from six different networks: LvSMA (SMN), RPreCun, and LAG (DMN), LSPL (FPN), LSTS (LAN), LPC (VAN), and RVP (VIS). The second mode, SM2 (Fig. 5 blue) consisted of regions from three networks: LPCC and Cun (DMN), RPreCun, and LPrCu (FPN), and RPOSd (VIS). The third mode SM3 (Fig. 5 red) instead involved only nodes from attention networks, namely LPreCun and RAC (VAN) and LpIPS (DAN). We suggest that these synchronized modes might represent a recurrent mechanism of temporal integration among higher-order RSNs such as DMN-FPN-SMN-LAN-VAN-VIS (SM1), DMN-FPN-VIS (SM2), and VAN-DAN (SM3). As far as it regards the alpha band, the same approach revealed no significant synchronization in this band.

After having localized clusters of synchronized hub regions in different modes, we investigated their temporal properties: frequency of occurrence, time of switch (ON/OFF within each mode), and transitions (among different modes). Firstly, SMs appear with a different frequency as measured with the proportion of ON epochs over the total time of recording. The pie-chart in Fig. 6**A** shows that SM1 (green), SM2 (blue), and SM3 (red) emerge 24%, 21%, and 18%, respectively, of the total time. The rest of the time (38%) none of these SMs are engaged (grey). We then inspected the temporal architecture of each SM (see Materials and Methods). Specifically, we analyzed the temporal distance (time lags) among ON epochs of each mode. This was estimated for each run and then statistically tested across runs, each time lag bin for every pair of modes. In general, all modes shared a common pattern (Fig. 6**B**) characterized by a stronger contribution of short temporal lags ([0.6–3] s, Fig. 6**B** dotted box). These findings together with the previous observations on the temporal occurrence, seem to suggest that hub regions alternate epochs of fast ON/OFF oscillations to long OFF epochs. In particular, at short temporal lags, the amplitude of SM3 bins resulted significantly higher than all the other modes ($p < 0.05$). This result combined with the lower frequency of occurrence (Fig. 6**A** red) suggests that SM3, as compared to the other modes, is less central over time, but during time intervals of significant centrality, it is characterized by a quicker temporal alternation.

Secondly, to characterize the synchronization model, SM temporal properties were linked to their switching, i.e. their transition probabilities defined on how ON periods alternated over time across modes. The transition between mode *i* and *j* corresponds to when a switch ON/OFF of mode *i* is followed by a switch OFF/ON of mode *j*. How often we observe such transitions, normalized by the total number of observed transitions, leads to the transition probabilities P_{ij}, i.e. the conditional probability to switch from mode *i* into mode *j* (see Materials and Methods). Fig. 6**C** shows that these probabilities are not uniform, i.e. they indicate specific loops. When SM1 is ON, it is very likely to switch to SM2 (P_{12} = 0.8). From SM2 it is almost certain to get back to SM1 (P_{21} = 0.99). This suggests a predominant loop between SM1 and SM2,

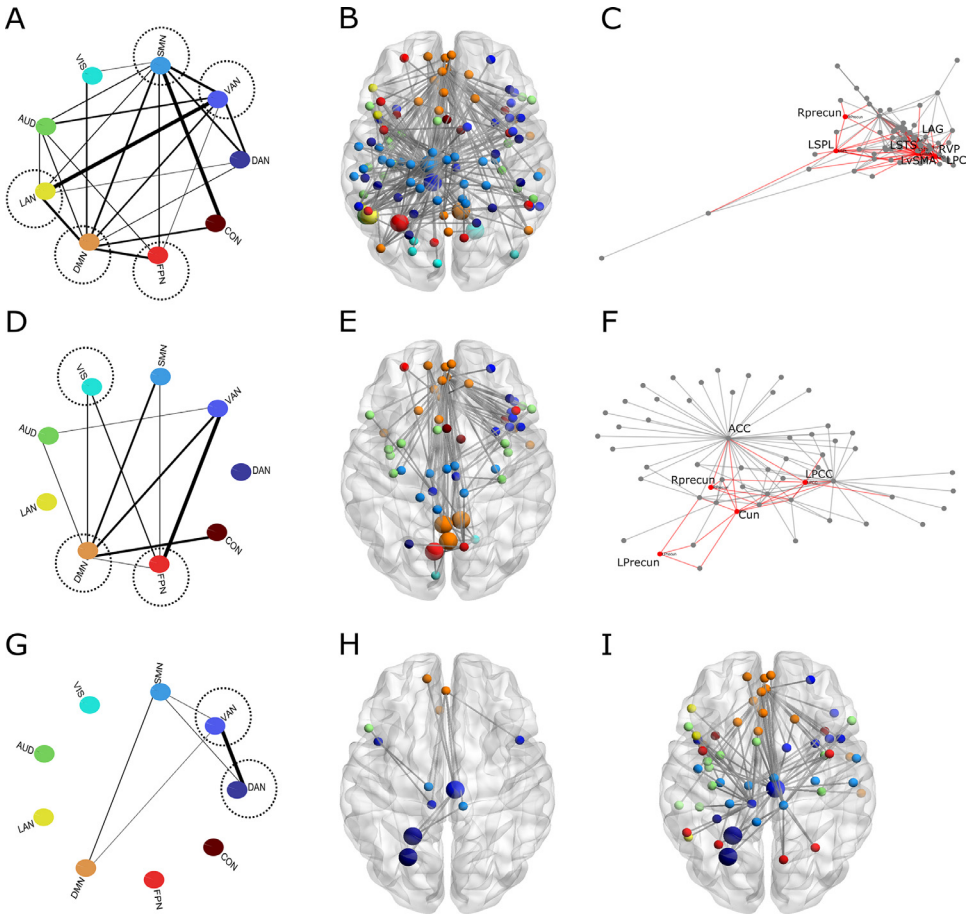

Fig. 7. Functional architecture during synchronization modes. The most stable connections over time are reported, i.e. connections present more than 95% of time during each ON epochs of SMs. The linewidth represents the percentage of time each connection is observed. A) During SM1 synchronization, the most stable connections involve DMN, SMN, FPN, LAN, and VAN. The VIS network establishes less frequent connections with the rest of the brain. B) The architecture of stable connections shows a high density of links covering uniformly the whole brain. C) The topography of these connections is represented through a spring-embedded graph. It can be noted that, as expected, the core of integration (red links) is represented by the SM1 hubs that realize a large number of stable connections. D) During SM2 synchronization stable connections involve mainly the DMN and FPN connecting them with the other RSNs. Of note, DAN and LAN are not included in the most stable connections. E) SM2 integration is realized through an anterior-posterior axis along the medial wall and the lateral frontal cortex. F) The topography of the spring embedded graph shows how this integration gravitates around two strong waystations: the pCC-Cun and the ACC areas. G) During SM3 synchronization a higher instability of connections is observed. The involved RSNs DAN-VAN are integrated among themselves and to a smaller extent involve DMN and SMN. H) This corresponds to a very sparse number of links exceeding the 95% percentile. This mode is characterized by more versatile connections. I) The connections observed in 50% of SM3 epochs show how the graph is highly integrated. This is in line with the previous observations on occurrence and transition probability involving this mode.

illustrated by the thick arrows in Fig. 6**C**. SM3 is only reached with a 20% probability from SM1. Once in SM3, the transition toward SM1 is more likely (around 70%) than toward SM2 ($P_{32} = 0.3$). Thus, SM3 less likely alternates with other modes and always through SM1.

The next analysis examined the spatial architecture of connections of each SM. Since SMs are based on the BC temporal alignment of the involved hubs and thus their connections can vary over time, we considered the most stable connections in each mode obtained from connectomes during their ON epochs. To characterize them, in Fig. 7 we report the topography of the most recurrent and consistent connections, i.e. occurring at 95% of synchronization time. In general, hub regions tend to be located along the medial wall of the hemisphere while 'peripheral' regions can be located both on the lateral and medial wall. The first column in Fig. 7 shows the graphs obtained from connectomes averaged across RSNs. The RSNs involved with every SM are circled and the linewidth represents the weight of the involved edges, i.e. the percentage of time each connection is observed. SM1 (Fig. 7**A**), formed by central regions across multiple RSNs, mainly involved other regions from these networks: DMN, SMN, FPN, LAN, and VAN. The VIS network, even though the visual region RVP is part of SM1, is less integrated. There is a strong integration axis between LAN, VAN, SMN, and CON, the latter not represented in the hub regions of SM1. The architecture of stable connections related to SM1 shows a high density of links covering uniformly the whole brain from the medial to the lateral wall (Fig. 7**B**). Fig. 7**C** shows the strength of connections through a spring embedded graph where the distance between nodes is inverse to their strength of connectivity. The red links show connections among SM1 hubs. Note the core of integration among hub regions with many stable connections. This is in line with the idea of a core network model, as suggested in (de Pasquale et al., 2016).

SM2 with hubs mainly in DMN and FPN includes a very different topography of connections with an anterior-posterior axis along the medial wall and the lateral frontal cortex (Fig. 7**D-E**). The architecture of SM2 connections extends to all other RSNs except DAN and LAN. The integration at the nodal level includes two medial wall regions: PCC-Cun and ACC (Fig. 7**E-F**).

SM3 (Fig. 7**G-I**) shows sparser stable connections that include a strong DAN-VAN integration, and a somehow weaker integration with SMN and DMN. It must be stressed that we are displaying only those connections exceeding the 95% percentile, thus these results do not suggest that this mode is less integrated but only that it exploits more versatile connections. In fact, when the threshold is lowered and connections above the 50% percentile (Fig. 7**I**), i.e. links present at least 50% of the time, are displayed, the graph is highly integrated. This is in line with the previous observations on occurrence and transition probability involving this mode. In summary, these analyses demonstrate that in the resting state a subset of hub regions becomes temporally synchronized (SMs). These SMs involve a specific combination of hub regions and peripheral connections with other regions, which identify temporal sequences of inter-regional synchronization that link different combinations of networks.

An important question is whether these SMs are relevant to global information processing in the brain at rest. We tried to address this question in two ways. First, we asked if whole-brain global efficiency (GE), a measure of efficient information transfer, fluctuates synchronously with the identified SMs. Second, we asked if artificial damage of such a small set of hub regions (less than 5% of the considered parcellation) significantly affects GE. We computed the Global Efficiency (GE, see Materials and Methods) averaged during the "ON" epochs, for all the identified modes. In Table 2 we report the average value of GE and of vulner-

Table 2
Synch modes seem to represent an efficient integration mechanism: on average the GE computed during the ON epochs is statistically higher (* p<0.01) than during the other epochs. The brain integration seems highly vulnerable (all SMs around 0.20 vulnerability) if these synchronization mechanisms are attacked.

	Sync Mode 1	Sync Mode 2	Sync Mode 3	Outside
Global Efficiency(within mode)	0.72 *	0.68 *	0.67 *	0.55 (* p<0.01)
Vulnerability(mode attacked within ON epochs)	0.2 *	0.19 *	0.19 *	-
Vulnerability*(mode attacked across time epochs)	0.18*	0.25*	0.36*	

ability averaged across the considered epochs. As shown in **Table 2**, GE resulted always statistically higher ($p < 0.01$) during "ON" epochs than outside, for all three modes. All modes resulted similarly efficient, namely GE = 0.72 (SM1) GE = 0.68 (SM2) and GE = 0.67 (SM3). This shows that SMs relate to a mechanism for more efficient integration. To address the vulnerability of the brain functional network concerning the failure of these hubs, we simulated two network attacks, as described in Materials and Methods. First, for each mode, during its temporal epochs of synchronous centrality, we statistically tested the vulnerability estimated when its hubs were removed vs. when the same number of hubs, uniformly sampled from the other static hubs (not in the considered mode) were removed (See Materials and Methods). Notably, even though hub regions included in each SM represent a very small fraction of all connectome nodes (<5%), we obtained statistically significant higher vulnerability, i.e. drops in efficiency close to 20%, for each SMs (**Table 2**). Second, we tested the vulnerability of the dynamic synchronization of the obtained SMs vs a set of fake SMs characterized by their FAKE-ON-epochs (see Materials and Methods). It can be noted that also, in this case, the results are encouraging, showing that for all SMs the vulnerability was statistically higher. Specifically, we obtained an increase of vulnerability of 0.18 for SM1, 0.25 for SM2, and 0.36 for SM3. It is interesting to note the slightly higher vulnerability obtained with SM3. This seems to suggest that, although composed of a fewer number of nodes, during its ON epochs SM3 acts like an important axis of integration, that is in line both with the observed transition probabilities and the topology of stable connections. These findings indicate that the overall efficiency is very vulnerable to this hub synchronization mechanism.

4. Discussion

We report a novel mechanism for network integration: in the beta band-limited power, a set of hubs synchronize their centrality, leading to three temporal modes of integration. These involve important nodes of higher cognitive domains such as internal cognition, executive control, somatomotor planning, language, and attention. They alternate over time with specific temporal properties and transition probabilities. This mechanism is highly efficient but also highly vulnerable to simulated lesions.

4.1. Temporal properties of the synchronization modes

The idea that synchronization modes might represent the resting brain's dynamic integration mechanism is in line with theoretical models. For example, in (Ponce-Alvarez et al., 2015), multiple clusters transiently synchronizing/desynchronizing emerge from the complex topology of anatomical connections. Our results emphasize the importance of hubs and fluctuating centrality in the integration and facilitation of information processing in terms of global efficiency. Specifically, global efficiency was always higher during "ON" epochs in a synchronization mode (SM), i.e., intervals of hub synchronization, compared to intervals in which the hubs were not synchronized (see Table 2). Moreover, replacing synchronized hubs belonging to a specific SM with non-synchronized hubs led to a statically significant vulnerability of around 20% efficiency loss. A similar vulnerability increase was obtained when comparing attacks to SM hubs during "ON" epochs and random "FAKE-ON" epochs. This finding is clinically significant since the global efficiency relates to cognitive performance, including better working memory in both children and adults, see for example (Stanley et al., 2015). Now, given the exiguous number of involved nodes, i.e., the most extensive SM1 mode included less than 5% of the connectome's nodes, the role played by temporal synchronization seems fundamental. To understand in more detail this mechanism, we addressed SM's temporal properties and their transition probabilities.

Different synchronization modes showed similar temporal behavior. They all stay "ON" a similar amount of time (around 20%, see Fig. 6**A**) mainly for short periods (Fig. 6**B**). Hence hub regions alternate epoch of fast ON/OFF oscillations to long OFF epochs. This fast switching is more pronounced for SM3, which has a density of shorter time lags significantly higher than the other modes hence a more frequent switch time. This property may reflect the component nodes' neural dynamics belonging mainly to the dorsal and ventral attention networks involved in attention control (Corbetta et al., 2008; Corbetta and Shulman, 2002). Furthermore, the slower temporal properties of synch modes 1 and 2 may relate to core-periphery models (Gollo et al., 2017). Gollo and colleagues observed that core regions, when perturbed through transcranial magnetic stimulation, fluctuate at lower frequencies than peripheral regions (Gollo et al., 2017). Thus, the inhibition of a core leads to further slowing that will lead to functional disconnection. In contrast, the excitation of a core region leads to higher oscillatory frequencies closer to peripheral regions, which will, in turn, increase global connectivity. Since core regions are densely connected, this mechanism will have a widespread impact on the overall brain network integration (Gollo et al., 2017). These considerations may help explain some of the temporal features and relationship to global efficiency that we observed. If hubs indeed tick at a slower frequency than peripheral regions, then hubs and peripheral regions are independent most of the time. However, periods of hub centrality will lead to a short burst of core-periphery synchronization, hence global efficiency peaks. The integration among networks is particularly strong during SM1's ON epochs. SM1 includes the most extensive set of hub regions belonging to different networks and the largest number of peripheral connections. These hubs include regions in networks that mediate the main cognitive domains, including internal cognition, language, attention, sensory-motor, and task control. SM2 mainly involves DMN hub regions, whose topography corresponds to the anatomical backbone of core regions described in diffusion anatomical studies (de Pasquale et al., 2012; de Pasquale et al., 2016; van den Heuvel and Sporns, 2011). Therefore, SM1-SM2-SM3 differ in their topography and temporal features, with SM1 being the slower and most static in terms of external connections and SM3 being faster with more varying connections (see Fig. 7). The variability of functional connections to/from the ventral attention network, in line with their tendency to couple with regions from other networks, is also apparent in static functional connectivity (fMRI) parcellation studies (Hacker et al., 2013; Power et al., 2011).

SMs also differ in their transition probabilities (Fig. 6**C**), which define temporal loops similar to what was reported in (Vidaurre et al., 2017). When the system is in the multi-network SM1, it is more likely to go in the DMN/FPN-SM2, and then return to the multi-network SM1. However, with a probability of about 30% SM1 can go to DAN/VAN-SM3, which is more likely to return to the multi-network SM1. Thus, the observed loops are in order of likelihood, SM1-SM2-SM1 followed

by SM1-SM3-SM1 and SM1-SM3-SM2-SM1. These SM3 transitions are in line with the observations reported in (Gu et al., 2015) where regions of the DAN and VAN are assigned the role of steering the system into states where different cognitive systems are either coupled or decoupled. In fact, from SM3 we either switch to SM1, a high integration mode among different cognitive systems (coupled), or SM2 where such broad integration only occurs through connections across the DMN-DAN-VAN (analogous to decoupled).

Furthermore, these observations can be related to the work of (Baker et al., 2014), where in terms of Hidden Markov Models it was reported that from a "DMN" state the transition to a "DAN" state was very unlikely. The authors linked these results to the original anti-correlation observed between these two networks (Fox et al., 2005). We believe that, based on our evidence on cross-network interactions, this anti-coupling among these networks is very unlikely. However, our current results extend this to the temporal domain, i.e. in terms of temporal alternation among these systems. Notably, we must highlight that our results do not refer to the RSN occurrence but their synchronization involving specific RSN hubs. Thus, while the widespread synchronization represented by SM1 continuously alternate with SM2 involving the "internal" DMN-FPN synchronization, the switching into the dorsal-ventral attention synchronization happens more rarely, and always from SM1 and never from SM2. This seems to suggest a specific directionality in mode switching, i.e. only from attentional into DMN-FPN systems. The directionality of these sequences will need to be verified in task conditions, an important development for the future.

In general, caution must be taken in linking SMs and HMM brain states, as originally defined in (Baker et al., 2014). First, they rely on different signals: the BLP (for the SMs) and the activity (for HMM), and thus they intrinsically focus on a slow vs a fast dynamic respectively. Second, the assumptions underlying the definition of states are very different, e.g. HMM states are mutually exclusive, they are based on a specific probabilistic model, the number of states is fixed a priori, etc. However, we believe that apart from the technical aspects, these approaches provide complementary information on the dynamics of communication in the brain. HMM states represent the dynamics of independent patterns of connectivity that can be related to the underlying RSNs. On the contrary, SMs relate to states of maximal integration across the different networks. They are obtained not only by extracting hubs, thus waystations of integration, but then looking at how these hubs are synchronized over time. SMs represent a specific mechanism of integration based on the synchronization of central structures. For this reason, SMs could be interpreted as a mechanism that allows the switching among the different HMM states (see above). However, apart from the technical aspects mentioned above, due to the opposite underlying assumptions (independence vs integration), we do not expect HMM and SMs to be similar but complementary. As a matter of fact, for example, the Posterior Cingulate and Precuneus that are largely represented in the obtained SMs were not obtained in any HMM states as discussed in (Baker et al., 2014). This is probably due to the fact this region is shared across multiple states and thus not assigned to any of them. Furthermore, it has been reported that the lack of representation of these two regions can be actually explained by the use of beamforming for source reconstruction. The basic mechanism is demonstrated in (Sjogard et al., 2019) where the application of the HMM combined with MNE does lead to a state that encompasses the posterior cingulate cortex and precuneus, see (Coquelet et al., 2020; Puttaert et al., 2020; Sjogard et al., 2019). However, to develop a Hidden Markov model where the hidden variable represents the occurrence of a state of integration driven by some measure of centrality, instead of brain activity, represents an interesting development of these techniques.

4.2. The topography of synchronization modes

Herein, we will describe the principal regions of each SM. Synch mode 1 includes hubs from multiple networks, including right Precuneus and left Angular Gyrus (DMN), left SPL (FPN), left ventral SMA (SMN), left superior temporal gyrus (LAN), left precuneus (VAN), and right ventro-parietal (VIS) (Fig. 5). This set of mainly medial regions, according to recent theories, sits at the top of the cortical hierarchy equidistant from unimodal systems (Vatansever et al., 2015; Wens et al., 2019), integrating across multiple sensory modalities (Margulies et al., 2016).

Functionally, some regions play a role in cross-network integration, e.g. precuneus in the DMN (de Pasquale et al., 2016; van den Heuvel and Sporns, 2011), and SMA in SMN (de Pasquale et al., 2012; de Pasquale et al., 2016; de Pasquale et al., 2013). The present work, however, shows that this integration might be realized through the temporal alignment of the respective RSN hubs. Other regions/networks that have been associated with high-level control include the FPN, which is related to task maintenance and coordination (Marek and Dosenbach, 2018), and that contributes through co-fluctuations with other networks to task control (Marek et al., 2015; Power et al., 2011; Power et al., 2013) (Sestieri et al., 2017), cognitive functioning (Sheffield et al., 2015), intelligence, and overall cognitive ability scores (Cole et al., 2015; Hearne et al., 2016).

Synch mode 2 includes nodes from DMN-FPN clustered around the Posterior Cingulate/Precuneus (Fig. 5). Notably, although this mode is more circumscribed, periods of high hub centrality recruit anterior parts of the medial frontal cortex that correspond to nodes of the SMN and CON in addition to DMN and FPN (**Fig. 7**). This anterior-posterior functional interaction nicely links with the strong anatomical anterior-posterior medial backbone found in anatomical studies (de Pasquale et al., 2017).

Given that the temporal overlap of SM1 and SM2 is negligible, these two modes may represent a mechanism of alternation between lateral sensory-motor cognitive vs. medial limbic networks, with the DMN in between, according to recent work on cortical gradients (Margulies et al., 2016).

Finally, synch mode 3 includes exclusively nodes of the DAN and VAN (Fig. 5). The dorsal and ventral attention systems largely segregated at rest communicate during re-orienting to environmental behaviorally relevant events and may be necessary for switching task states (Corbetta et al., 2008). Notably, the more stable connections found during epochs of significant centrality involve only these two networks (Fig. 7).

4.3. The role of DMN and network controllability

The DMN is largely represented in the identified SMs (around 30% of the observed nodes are from DMN) with regions of PCC/Precuneus falling into distinct modes. Parcels of the posterior cingulate, although spatially very close, seem to be characterized by a different dynamic of centrality. This suggests a distinct functional specialization in these areas. Such a fine-scale organization can be related to previous fMRI results, see for example Preti and Van De Ville (2017) where connectivity patterns, driven by the dynamics of the eigenvector centrality, link the ventral part of the precuneus with DMN, FPN, and LAN. Such topography is well in agreement with SM1 apart from the contribution of SMN, through the node LvSMA. This node in Preti and Van De Ville (2017) was still associated with precuneus, but its dorsal region in a cluster whose projections included the anterior salience, temporal and visual areas. Further, in our case, parts of the Precuneus (LPreCun) were also involved in the DAN-VAN integration represented by SM3, and in SM1 and SM2 different parcels of the PreCuneus were linked to visual nodes. Such synchronization of DMN subsystems through different temporal dynamics can be linked to the reported functional heterogeneity of this network which plays an intricate interplay among RSNs (Christoff et al., 2016; Yang et al., 2014), related for example to task engagement and goal-directed thoughts, thus more complex than just task-positive/negative networks (Fox et al., 2005).

However, an important difference between our work and Preti and Van De Ville (2017) is that the latter analyzed the consistency of hub

connections over time and not their direct temporal synchronization. We believe instead that this property might be fundamental in ensuring an efficient integration in the brain. Several studies point in this direction. For example, in an EEG study (Kabbara et al., 2017), DMN hubs are found to alternate over time their role from connector (global) to provincial (local) hubs. This alternation seems to relate to network vulnerability. These EEG findings are in agreement with our MEG results (Table 2). Analogously to (Kabbara et al., 2017), our hubs alternate their role of global integration. However, this does not relate to the centrality of a single node, but to a consensus of hubs aligned over time. Since this alignment is time-varying we could speculate that in the temporal epochs where these nodes are not aligned, they switch to a more provincial role, in analogy to (Kabbara et al., 2017).

Also in (Vatansever et al., 2015), the DMN is reported as a flexible RSN involved in higher cognitive processing, whose hubs switch continuously community membership in terms of nodal participation coefficient and strength. Also, in this case, the authors suggest for DMN a role in conscious processing that is in line with our findings on this role could be related to the link to other RSNs, e.g. FPN and SMN, and realized through independent axes of temporal synchronization.

Eventually, we might link the observed topography of all SMs to the observations of Gu and colleagues (Gu et al., 2015) on how the brain moves among cognitive states, driven by a property called network controllability. They report that, based on Diffusion Spectrum Imaging, DMN areas, the posterior cingulate and precuneus, are involved in facilitating the movement of the brain to many easily reachable states (average controllability). On the other hand, regions in cognitive control systems, such as FPN and CON, are found to facilitate the movement of the brain towards difficult-to-reach states (modal controllability). Notably, in our study, the temporal synchronization of hubs seems to suggest that average and modal controllability exploit the same integration axis represented by SM1, where these systems are grouped. Further, in (Gu et al., 2015) regions of the DAN and VAN are assigned the role of steering the brain into states where different cognitive systems are either coupled or decoupled. This observation nicely links with the observed transition probabilities and loops among SMs discussed above.

4.4. Link to the dynamic core network in the beta band

The identified SMs were specific for the beta band (**Fig. 2**), not the alpha band (**Fig. 3**). This band specificity is in line with our previous work on beta band power fluctuations in across-RSNs interactions. In fact, since our first observations on the MEG dynamics of RSNs, we reported a similar topography of RSN networks in the alpha and beta band (see for example (de Pasquale et al., 2010)). However, when the across network interactions were studied, the alpha band resembled the architecture observed in the beta band with reduced importance. For example, in alpha, the DMN resulted central as well as the PCC but with a lower degree as compared to the beta band (de Pasquale et al., 2012). This is in line with what was reported in (Wens et al., 2019) and with the integration role played by the beta band in the “prior” hypothesis proposed in (Betti et al., 2021). Besides, also in (Della Penna et al., 2019) where alpha vs beta-band functional hubs were compared, we observed some agreement. In this case, the number of hubs was even higher than the hubs found in the beta band (note that a different analysis strategy was employed as compared to this work). However, the temporal dynamics of centrality in these two bands seem very different. In this work, the identified hubs in alpha did not show any significant synchronization. This difference between alpha and beta is also in line with previous studies, see for example (Betti et al., 2018). Here we observed that while in the beta band the dynamics of centrality were maintained during rest and a naturalistic stimulus, this did not apply to the alpha band linking this band to the idling hypothesis, see (Raichle, 2011). On the other hand, the similarity between rest and natural vision beta band fluctuations could be interpreted to represent temporal priors to visual scene processing (Betti et al., 2018).

Finally, we have reported on a beta-band dynamic core’ or a set of hub regions whose synchronization fluctuates in synch with whole-brain global efficiency (de Pasquale et al., 2016). Those hubs, obtained from a much smaller graph, correspond in part to those found in the current study, e.g. PCC, SMA, and LpIPS. The current work provides a more general account of hub dynamics and their effect on efficiency. We computed centrality on whole-brain fully connected networks using an entirely data-driven approach. In contrast, previously, hub dynamics were computed on specific networks and in temporal epochs of strong within-RSN correlation (de Pasquale et al., 2010).

4.5. Independent hubs and remote synchronization

It must be noted that our analysis focused on a specific aspect of hub dynamics: the synchronization of hub centrality which represents only a part of the complex hub dynamics. Thus, the obtained low dimensionality of SMs is not surprising. In fact, in this scenario hubs with an independent dynamic are not included. Furthermore, also hubs whose synchronization fluctuates among a different set of hubs (not the same over time) do not fall in the synch mode description. Further, SMs themselves are not always engaged but only around 20% of the time. This seems to suggest that, although this mechanism is very important on the overall communication, still a consistent part of it might be explained the other kind of hub dynamics. In fact, for example, a large proportion (40%) of the identified hubs did not synchronize their centrality and remained mostly independent. Then this independent set of hubs contributes to brain integration using a different mechanism. One of such mechanisms may be ’remote synchronization’ Vlasov and Bifone (2017). This phenomenon, first observed in a star network of oscillators, explains the synchronization of unconnected peripheral nodes through a hub that maintains its independent dynamics. This mechanism might be an exciting development for future work.

4.6. Metastability and pulsatility

We speculate that this study’s pulsatile integration might be related to brain models operating at a critical regime (Cocchi et al., 2017). In analogy with the idea that the brain behaves as a metastable system visiting different states over time, we found that the brain visits few synchronization modes alternating over time in terms of integration. We speculate that these SMs represent a mechanism that allows state shifts.

4.7. Methodological considerations

There are several critical methodological aspects to discuss concerning ours and others’ previous work (de Pasquale et al., 2010; de Pasquale et al., 2012; de Pasquale et al., 2016).

First, in this study, we applied a signal leakage correction to the MEG signals by adopting the Geometric Correction scheme developed by (Wens et al., 2015) (Della Penna et al., 2019). This correction minimizes the impact of spurious correlations in MEG BLP data and thus the topology of functional connectivity (Della Penna et al., 2019). Further, we adopted a dense parcellation scheme based on 155 nodes extracted from 9 RSNs. This higher density of nodes (42 nodes and 6 RSNs in (de Pasquale et al., 2016)) allows for complete brain network coverage. The parcellation scheme affects the graph analysis and other parameters, such as the threshold for functional connectomes’ binarization. We minimized any manual selection as all the thresholds applied to the functional connectomes and Betweenness Centrality relied on specific null models from bootstrapping. Also, as suggested in (Bordier et al., 2017), we required a fully connected connectome, where each node can be reached by any other. This choice produces more homogenous graphs in terms of architecture but a variable density that might affect the centrality estimation.

Another important aspect is the adoption of Betweenness Centrality. Several measures can be adopted to quantify functional hubs, however, the set of hub nodes identified in this study have been consistently reported as functional hubs across imaging modalities and different centrality measures, as discussed in (de Pasquale et al., 2018).

Credit author statement

F. de Pasquale: Conceptualization, Data curation, Formal analysis, Investigation, Methodology, Project administration, Resource, Software, Supervision, Validation, Visualization, Writing - original draf, Writing - review & editing. **S. Spadone**: Data curation, Supervision, Writing - review & editing. **V. Betti**: Data curation, Supervision, Writing - review & editing. **M. Corbetta**: Conceptualization, Methodology, Supervision, Writing - original draf, Writing - review & editing. **S. Della Penna**: Conceptualization, Data curation, Formal analysis, Investigation, Methodology, Software, Supervision, Validation, Visualization, Writing - original draf, Writing - review & editing.

Data codes availability

The data and developed codes that support the findings of this study are available from the corresponding author, Francesco de Pasquale (FdP), upon reasonable request .

Acknowledgements

FdP was partially funded within the "Demetra" Project (Departments of Excellence 2018-2022, CUP _C46C18000530001), funded by the Ministry of Education, University and Research;SDP and SS were partially supported by the “Departments of Excellence 2018-2022” initiative of the Italian Ministry of Education, University and Research for the Department of Neuroscience, Imaging and Clinical Sciences (DNISC) of the University of Chieti-Pescara.

References

Baker, A.P., Brookes, M.J., Rezek, I.A., Smith, S.M., Behrens, T., Probert Smith, P.J., Woolrich, M., 2014. Fast transient networks in spontaneous human brain activity. Elife 3, e01867.

Baldassarre, A., Ramsey, L., Hacker, C.L., Callejas, A., Astafiev, S.V., Metcalf, N.V., Zinn, K., Rengachary, J., Snyder, A.Z., Carter, A.R., Shulman, G.L., Corbetta, M., 2014. Large-scale changes in network interactions as a physiological signature of spatial neglect. Brain 137, 3267–3283.

Bastian, M., Heymann, S., Jacomy, M., 2009. Gephi: an open source software for exploring and manipulating networks. International AAAI Conference on Weblogs and Social Media.

Betti, V., Corbetta, M., de Pasquale, F., Wens, V., Della Penna, S., 2018. Topology of functional connectivity and hub dynamics in the beta band as temporal prior for natural vision in the human brain. J. Neurosci. 38, 3858–3871.

Betti, V., Della Penna, S., de Pasquale, F., Corbetta, M., 2021. Spontaneous beta band rhythms in the predictive coding of natural stimuli. The Neuroscientist.

Bordier, C., Nicolini, C., Bifone, A., 2017. Graph analysis and modularity of brain functional connectivity networks: searching for the optimal threshold. Front. Neurosci. 11, 441.

Brookes, M., Woolrich, M., Luckhoo, H., Price, D., Hale, J.R., Stephenson, M.C., Barnes, G.R., Smith, S.M., Morris, P.G., 2011. Investigating the electrophysiological basis of resting state networks using magnetoencephalography. Proc. Natl. Acad. Sci. USA 108, 16783–16788.

Chang, C., Glover, G.H., 2010. Time-frequency dynamics of resting-state brain connectivity measured with fMRI. Neuroimage 50, 81–98.

Christoff, K., Irving, Z.C., Fox, K.C., Spreng, R.N., Andrews-Hanna, J.R., 2016. Mind-wandering as spontaneous thought: a dynamic framework. Nat. Rev. Neurosci. 17, 718–731.

Cocchi, L., Gollo, L.L., Zalesky, A., Breakspear, M., 2017. Criticality in the brain: a synthesis of neurobiology, models and cognition. Prog. Neurobiol. 158, 132–152.

Cole, M.W., Ito, T., Braver, T.S., 2015. Lateral prefrontal cortex contributes to fluid intelligence through multinetwork connectivity. Brain Connect. 5, 497–504.

Cole, M.W., Reynolds, J.R., Power, J.D., Repovs, G., Anticevic, A., Braver, T.S., 2013. Multi-task connectivity reveals flexible hubs for adaptive task control. Nat. Neuroscience. 16, 1348–1355.

Coquelet, N., Wens, V., Mary, A., Niesen, M., Puttaert, D., Ranzini, M., Vander Ghinst, M., Bourguignon, M., Peigneux, P., Goldman, S., Woolrich, M., De Tiege, X., 2020. Changes in electrophysiological static and dynamic human brain functional architecture from childhood to late adulthood. Sci. Rep. 10, 18986.

Corbetta, M., Patel, G., Shulman, G.L., 2008. The reorienting system of the human brain: from environment to theory of mind. Neuron 58, 306–324.

Corbetta, M., Shulman, G.L., 2002. Control of goal-directed and stimulus-driven attention in the brain. Nat. Rev. Neurosci. 3, 201–215.

de Pasquale, F., Corbetta, M., Betti, V., Della Penna, S., 2018. Cortical cores in network dynamics. Neuroimage 180, 370–382.

de Pasquale, F., Della Penna, S., Sabatini, U., Caravasso Falletta, C., Peran, P., 2017. The anatomical scaffold underlying the functional centrality of known cortical hubs. Hum Brain Mapp. 38, 5141–5160.

de Pasquale, F., Della Penna, S., Snyder, A.Z., Lewis, C., Mantini, D., Marzetti, L., Belardinelli, P., Ciancetta, L., Pizzella, V., Romani, G.L., Corbetta, M., 2010. Temporal dynamics of spontaneous MEG activity in brain networks. Proc. Natl. Acad. Sci. USA 107, 6040–6045.

de Pasquale, F., Della Penna, S., Snyder, A.Z., Marzetti, L., Pizzella, V., Romani, G.L., Corbetta, M., 2012. A cortical core for dynamic integration of functional networks in the resting human brain. Neuron 74, 753–764.

de Pasquale, F., Della Penna, S., Sporns, O., Romani, G.L., Corbetta, M., 2016. A dynamic core network and global efficiency in the resting human brain. Cereb Cortex 26, 4015–4033.

de Pasquale, F., Sabatini, U., Della Penna, S., Sestieri, C., Caravasso, C., Formisano, R, P., P., 2013. The connectivity of functional cores reveals different degrees of segregation and integration in the brain at rest. Neuroimage 69, 51–61.

Della Penna, S., Corbetta, M., Wens, V., de Pasquale, F., 2019. The impact of the geometric correction scheme on MEG functional topology at rest. Front. Neurosci. 13, 1114.

Della Penna, S., Del Gratta, C., Granata, C., Pasquarelli, A., Pizzella, V., Rossi, R., Russo, M., Torquati, K., Ernè, S.N., 2000. Biomagnetic systems for clinical use. Philosophical Magazine B 80 (5), 937–948. doi:10.1080/01418630008221960.

Favaretto, C., Spadone, S., Sestieri, C., Betti, V., Cenedese, A., Della Penna, S., Corbetta, M., 2021. Multi-band MEG signatures of BOLD connectivity reorganization during visuospatial attention. Neuroimage 230, 117781.

Fawcett, T., 2006. An introduction to ROC analysis. Pattern Recogn. Lett. 27, 13.

Fox, M.D., Snyder, A.Z., Vincent, J.L., Corbetta, M., Van Essen, D.C., Raichle, M.E., 2005. The human brain is intrinsically organized into dynamic, anticorrelated functional networks. Proc. Natl. Acad. Sci. USA 102, 9673–9678.

Gollo, L.L., Roberts, J.A., Cocchi, L., 2017. Mapping how local perturbations influence systems-level brain dynamics. Neuroimage.

Gordon, E.M., Lynch, C.J., Gratton, C., Laumann, T.O., Gilmore, A.W., Greene, D.J., Ortega, M., Nguyen, A.L., Schlaggar, B.L., Petersen, S.E., Dosenbach, N.U.F., Nelson, S.M., 2018. Three distinct sets of connector hubs integrate human brain function. Cell Rep. 24, 1687–1695 e1684.

Gu, S., Pasqualetti, F., Cieslak, M., Telesford, Q.K., Yu, A.B., Kahn, A.E., Medaglia, J.D., Vettel, J.M., Miller, M.B., Grafton, S.T., Bassett, D.S., 2015. Controllability of structural brain networks. Nat. Commun. 6, 8414.

Hacker, C.D., Laumann, T.O., Szrama, N.P., Baldassarre, A., Snyder, A.Z., Leuthardt, E.C., Corbetta, M., 2013. Resting state network estimation in individual subjects. Neuroimage 82, 616–633.

Hearne, L.J., Mattingley, J.B., Cocchi, L., 2016. Functional brain networks related to individual differences in human intelligence at rest. Sci. Rep. 6, 32328.

Hipp, J.F., Hawellek, D.J., Corbetta, M., Siegel, M., Engel, A.K., 2012. Large-scale cortical correlation structure of spontaneous oscillatory activity. Nat. Neurosci. 15, 884–890.

Hutchison, R., Womelsdorf, T., Allen, E., Bandettini, P., Calhoun, V., Corbetta, M., Della Penna, S., Duyn, J., Glover, G., Gonzalez-Castillo, J., Handwerker, D., Keilholz, S., Kiviniemi, V., Leopold, D., de Pasquale, F., Sporns, O., Walter, M., Chang, C., 2013. Dynamic functional connectivity: promise, issues, and interpretations. Neuroimage 80, 18.

Kabbara, A., El Falou, W., Khalil, M., Wendling, F., Hassan, M., 2017. The dynamic functional core network of the human brain at rest. Sci. Rep. 7, 2936.

Larson-Prior, L.J., Oostenveld, R., Della Penna, S., Michalareas, G., Prior, F., Babajani-Feremi, A., Schoffelen, J.M., Marzetti, L., de Pasquale, F., Di Pompeo, F., Stout, J., Woolrich, M., Luo, Q., Bucholz, R., Fries, P., Pizzella, V., Romani, G.L., Corbetta, M., Snyder, A.Z.Consortium, W.U.-M.H., 2013. Adding dynamics to the human connectome project with MEG. Neuroimage 80, 190–201.

Mantini, D., Della Penna, S., Marzetti, L., de Pasquale, F., Pizzella, V., Corbetta, M., Romani, G.L., 2011. A signal-processing pipeline for magnetoencephalography resting-state networks. Brain Connect. 1, 49–59.

Marek, S., Dosenbach, N.U.F., 2018. The frontoparietal network: function, electrophysiology, and importance of individual precision mapping. Dialogues Clin. Neurosci. 20, 133–140.

Marek, S., Hwang, K., Foran, W., Hallquist, M.N., Luna, B., 2015. The contribution of network organization and integration to the development of cognitive control. PLoS Biol. 13, e1002328.

Margulies, D.S., Ghosh, S.S., Goulas, A., Falkiewicz, M., Huntenburg, J.M., Langs, G., Bezgin, G., Eickhoff, S.B., Castellanos, F.X., Petrides, M., Jefferies, E., Smallwood, J., 2016. Situating the default-mode network along a principal gradient of macroscale cortical organization. Proc. Natl. Acad. Sci. USA 113, 12574–12579.

Marzetti, L., Della Penna, S., Snyder, A.Z., Pizzella, V., Nolte, G., de Pasquale, F., Romani, G.L., Corbetta, M., 2013. Frequency specific interactions of MEG resting state activity within and across brain networks as revealed by the multivariate interaction measure. Neuroimage 79, 172–183.

Ponce-Alvarez, A., Deco, G., Hagmann, P., Romani, G.L., Mantini, D., Corbetta, M., 2015. Resting-state temporal synchronization networks emerge from connectivity topology and heterogeneity. PLoS Comput. Biol. 11, e1004100.

Power, J.D., Cohen, A.L., Nelson, S.M., Wig, G.S., Barnes, K.A., Church, J.A., Vogel, A.C., Laumann, T.O., Miezin, F.M., Schlaggar, B.L., Petersen, S.E., 2011. Functional network organization of the human brain. Neuron 72, 665–678.

Power, J.D., Schlaggar, B.L., Lessov-Schlaggar, C.N., Petersen, S.E., 2013. Evidence for hubs in human functional brain networks. Neuron 79, 798–813.
Preti, M.G., Van De Ville, D., 2017. Dynamics of functional connectivity at high spatial resolution reveal long-range interactions and fine-scale organization. Sci. Rep. 7, 12773.
Prichard, D., Theiler, J., 1994. Generating surrogate data for time series with several simultaneously measured variables. Phys. Rev. Lett. 73, 951–954.
Puttaert, D., Coquelet, N., Wens, V., Peigneux, P., Fery, P., Rovai, A., Trotta, N., Sadeghi, N., Coolen, T., Bier, J.C., Goldman, S., De Tiege, X., 2020. Alterations in resting-state network dynamics along the Alzheimer's disease continuum. Sci. Rep. 10, 21990.
Raichle, M.E., 2011. The restless brain. Brain Connect. 1, 3–12.
Rubinov, M., Sporns, O., 2010. Complex network measures of brain connectivity: uses and interpretations. Neuroimage 52, 1059–1069.
Sebastiani, V., de Pasquale, F., Costantini, M., Mantini, D., Pizzella, V., Romani, G.L., Della Penna, S., 2014. Being an agent or an observer: different spectral dynamics revealed by MEG. Neuroimage 102 (Pt 2), 717–728.
Sestieri, C., Shulman, G.L., Corbetta, M., 2017. The contribution of the human posterior parietal cortex to episodic memory. Nat. Rev. Neurosci. 18, 183–192.
Sheffield, J.M., Repovs, G., Harms, M.P., Carter, C.S., Gold, J.M., MacDonald 3rd, A.W., Daniel Ragland, J., Silverstein, S.M., Godwin, D., Barch, D.M., 2015. Fronto-parietal and cingulo-opercular network integrity and cognition in health and schizophrenia. Neuropsychologia 73, 82–93.
Shine, J.M., Bissett, P.G., Bell, P.T., Koyejo, O., Balsters, J.H., Gorgolewski, K.J., Moodie, C.A., Poldrack, R.A., 2016. The dynamics of functional brain networks: integrated network states during cognitive task performance. Neuron 92, 544–554.
Shine, J.M., Breakspear, M., Bell, P.T., Ehgoetz Martens, K.A., Shine, R., Koyejo, O., Sporns, O., Poldrack, R.A., 2019. Human cognition involves the dynamic integration of neural activity and neuromodulatory systems. Nat. Neurosci. 22, 289–296.
Sinibaldi, R., Conti, A., Sinjari, B., Spadone, S., Pecci, R., Palombo, M., Komlev, V.S., Ortore, M.G., Tromba, G., Capuani, S., Guidotti, R., De Luca, F., Caputi, S., Traini, T., Della Penna, S., 2018. Multimodal-3D imaging based on muMRI and muCT techniques bridges the gap with histology in visualization of the bone regeneration process. J. Tissue Eng. Regen. Med. 12, 750–761.
Sjogard, M., De Tiege, X., Mary, A., Peigneux, P., Goldman, S., Nagels, G., van Schependom, J., Quinn, A.J., Woolrich, M.W., Wens, V., 2019. Do the posterior midline cortices belong to the electrophysiological default-mode network? Neuroimage 200, 221–230.
Spadone, S., de Pasquale, F., Mantini, D., Della Penna, S., 2012. A K-means multivariate approach for clustering independent components from magnetoencephalographic data. Neuroimage 62, 1912–1923.
Stanley, M.L., Moussa, M.N., Paolini, B.M., Lyday, R.G., Burdette, J.H., Laurienti, P.J., 2013. Defining nodes in complex brain networks. Front. Comput. Neurosci. 7, 169.
Stanley, M.L., Simpson, S.L., Dagenbach, D., Lyday, R.G., Burdette, J.H., Laurienti, P.J., 2015. Changes in brain network efficiency and working memory performance in aging. PLoS One 10, e0123950.
Van de Ville, D., Britz, J., Michel, C.M., 2010. EEG microstate sequences in healthy humans at rest reveal scale-free dynamics. Proc. Natl. Acad. Sci. USA 107, 18179–18184.
van den Heuvel, M.P., Sporns, O., 2011. Rich-club organization of the human connectome. J. Neurosci. 31, 15775–15786.
van den Heuvel, M.P., Sporns, O., 2013. Network hubs in the human brain. Trends Cogn. Sci. 17, 683–696.
Vatansever, D., Menon, D.K., Manktelow, A.E., Sahakian, B.J., Stamatakis, E.A., 2015. Default mode dynamics for global functional integration. J. Neurosci. 35, 15254–15262.
Vidaurre, D., Smith, S.M., Woolrich, M.W., 2017. Brain network dynamics are hierarchically organized in time. Proc. Natl. Acad. Sci. USA 114, 12827–12832.
Vlasov, V., Bifone, A., 2017. Hub-driven remote synchronization in brain networks. Sci. Rep. 7, 10403.
Wens, V., 2015. Investigating complex networks with inverse models: Analytical aspects of spatial leakage and connectivity estimation. Phys. Rev. E Stat. Nonlinear Soft Matter Phys. 91, 012823.
Wens, V., Bourguignon, M., Vander Ghinst, M., Mary, A., Marty, B., Coquelet, N., Naeije, G., Peigneux, P., Goldman, S., De Tiege, X., 2019. Synchrony, metastability, dynamic integration, and competition in the spontaneous functional connectivity of the human brain. Neuroimage 199, 313–324.
Wens, V., Marty, B., Mary, A., Bourguignon, M., Op de Beeck, M., Goldman, S., Van Bogaert, P., Peigneux, P., De Tiege, X., 2015. A geometric correction scheme for spatial leakage effects in MEG/EEG seed-based functional connectivity mapping. Hum Brain Mapp. 36, 4604–4621.
Yang, Z., Craddock, R.C., Margulies, D.S., Yan, C.G., Milham, M.P., 2014. Common intrinsic connectivity states among posteromedial cortex subdivisions: Insights from analysis of temporal dynamics. Neuroimage 93 Pt 1, 124–137.